Journal of Materials Chemistry A

ROYAL SOCIETY OF CHEMISTRY

PAPER

View Article Online
View Journal

Cite this: DOI: 10.1039/d5ta08384b

Investigating Ti–Nb alloys as supports for iridium oxide water oxidation electrocatalysts

Guangmeimei Yang, [ab] Wei Huang,[c] Yifeng Wang,[b] Caiwu Liang,[ab] Yuxiang Zhou,[b] Santosh Kumar,[d] Pilar Ferrer Escorihuela, [d] Parnia Navabpour,[e] Giuseppe Sanzone,[e] Trevor Ferris, [a] Mark Turner, [f] Sarah J. Haigh, [f] Georg Held, [d] Caterina Ducati,[c] Andreas Kafizas *[ag] and Reshma R. Rao *[bh]

The scarcity of Ir presents a major challenge for scaling up its use as a water oxidation electrocatalyst in proton exchange membrane (PEM) water electrolysers. Developing conductive and stable supports is an effective way to reduce iridium loading while maintaining performance. However, the influence of support conductivity and stability on Ir-based catalytic activity remains poorly understood. The behaviour of the support is often obscured in conventional membrane electrode assembly (MEA) systems because IrO_x itself is both highly conductive and exceptionally stable. To decouple support conductivity and passivation effects from the intrinsic conductivity of IrO_x, we demonstrate a screening platform by studying a series of Ti–Nb alloy thin films produced by sputter deposition and investigate their performance as supports for IrO_x water oxidation electrocatalysts. A range of electrochemical tests including accelerated stress tests (AST) were carried out on these samples, where characterisation techniques, including X-ray absorption spectroscopy (XAS), X-ray photoelectron spectroscopy (XPS) and high resolution transmission electron microscopy (HRTEM), demonstrated the *in situ* formation of passivation layers on these supports during water oxidation. Our results suggest that a ~10 nm oxide passivation layer forms on metallic Ti-based supports. On alloying Nb with Ti metal, a more insulating rutile TiO_2 phase forms during water oxidation whereas an anatase TiO_2, with higher conductivity, is observed on the pure Ti support. Consequently, although alloying Ti with Nb improves the bulk conductivity, the structure of the oxide passivation layer results in a drastic decrease of conductivity and water oxidation activity. Our results demonstrate the importance of the structure and composition of surface oxide phases formed during water oxidation in controlling the overall stability and conductivity of support materials.

Received 14th October 2025
Accepted 8th April 2026

DOI: 10.1039/d5ta08384b

rsc.li/materials-a

Introduction

Hydrogen plays a significant role both for the deployment of low carbon fuels and in chemical production. To sustainably meet growing demand, green hydrogen production needs to meet the target of 70–125 Mt per year by 2030, which is more than 100 times higher than the total production seen in 2022.[1] Proton exchange membrane (PEM) water electrolysis is one of the most promising technologies to generate green hydrogen using intermittent electricity from renewable sources, owing to its fast start-up and shut-down dynamics and high gas purity compared with alkaline water electrolysis and solid oxide electrolysis.[2] However, the bottleneck of scaling up PEM water electrolysers is the high stack cost, primarily due to the high iridium (Ir) loading (2–3 mg cm^{-2}) required for the electrocatalyst that drives the oxygen evolution reaction (OER) at the anode, as well as the use of platinum- or gold-coated titanium as the galvanic plate to endure anodic potentials and local acidity.[3] Ir is one of the scarcest metals in the Earth's crust; as PEM water electrolysers are scaled up, the capital cost of Ir will likely rise.[4] Moreover, with current Ir loading at 2–3 mg cm^{-2}, meeting the global energy demand on a terawatt scale will require several decades of sustained Ir production.[5] According to the U.S. Department of Energy technical targets, Ir loading in PEM water electrolysers should be reduced to below 0.5 mg cm^{-2} by 2026

[a]Department of Chemistry, Molecular Science Research Hub, Imperial College London, White City, W12 0BZ, London, UK. E-mail: a.kafizas@imperial.ac.uk

[b]Department of Materials, Imperial College London, South Kensington, SW7 2AZ, London, UK. E-mail: reshma.rao@imperial.ac.uk

[c]Department of Materials Science and Metallurgy, University of Cambridge, CB3 0FS, Cambridge, UK

[d]B07, Diamond Light Source, Harwell Science and Innovation Campus, Didcot OX11 0DE, UK

[e]Teer Coatings Ltd, West Stone, West Stone House, Droitwich WR9 9AS, UK

[f]Department of Materials, The University of Manchester, M13 9PL, Manchester, UK

[g]London Centre for Nanotechnology, Imperial College London, UK

[h]Grantham Institute – Climate Change and the Environment, Imperial College London, UK

and to 0.125 mg cm^{-2} ultimately, in order to enable large-scale green hydrogen production.[6] Simply reducing Ir loading down to 0.5 mg cm^{-2} will not resolve this issue, as it results in an inadequate inter-catalyst contact and limited in-plane conductivity due to the inhomogeneity of the catalyst layer, leading to a significant increase in operational voltage and even cell failure.[7,8]

One of the most practical approaches to reduce Ir loading without compromising on in-plane conductivity is to disperse Ir oxide (IrO_x) nanoparticles onto a stable, conductive and high surface area support.[9–11] Promising results for combined activity and stability have been reported for supported IrO_x compared with unsupported IrO_x.[9] Literature studies have widely investigated powder nanoparticle-based supports for OER.[9,12–14] However, using such samples, it is difficult to deconvolute the conductivity effect of the often less conductive support that is combined with IrO_2, which is a metallic conductor (Fig. 1A), where electrons will preferentially travel through the more conductive IrO_2 layer. This results in similar through-plane conductivity and OER activity which primarily depends on the loading and connectivity of the IrO_2.[15–17] To remove the complexity associated with variable surface area, in this work we fabricated thin film supports with well-defined surface area to investigate the effect of the conductivity of the support (Fig. 1B).

Possible conductive support materials, including doped tin oxides (SnO_2),[18–21] doped titanium oxides (TiO_2),[22–24] titanium suboxides (TiO_x)[25–27] and titanium nitrides (TiN_x),[28–31] have been extensively studied as a conductive support for IrO_x. Doped SnO_2 is an attractive candidate due its high conductivity and corrosion resistance,[19] but experimentation has shown they have insufficient stability at the required operating conditions for implementation in practical devices. Therefore, TiO_2 based materials remain the most popular explored candidates. However, TiO_2 is intrinsically highly insulating, and when combined with IrO_x, requires a high level of doping to show sufficient conductivity to function, limiting the efficient utilisation of IrO_x.[22,32–34]

Niobium (Nb) is alloyed with Ti to stabilise and improve the corrosion resistance of the β-phase in Ti–Nb alloys.[35] In addition, the conductivity of TiO_2 can be significantly enhanced when doped with Nb.[36,37] It is generally proposed that Nb^{5+} cations substitute Ti^{4+} sites resulting in an increase in electron donors in the system, which can lead to orders of magnitude increases in conductivity compared with undoped TiO_2.[38–40]

Inspired by the excellent corrosion-resistance behaviour and superior conductivity of Ti–Nb alloys, here we investigate the potential of Nb alloyed Ti supports for the OER. We use sputter deposition to synthesise a series Ti–Nb alloy thin films with varying Nb content (0, 5, 10, 20, 50 and 100 at%) and assess their suitability for supporting IrO_x for the OER using a suite of electrochemical methods and advanced *ex situ* characterisation (four-point probe, cross-section transmission electron microscopy, X-ray absorption spectroscopy (XAS), X-ray photoelectron spectroscopy (XPS) and inductively coupled plasma mass

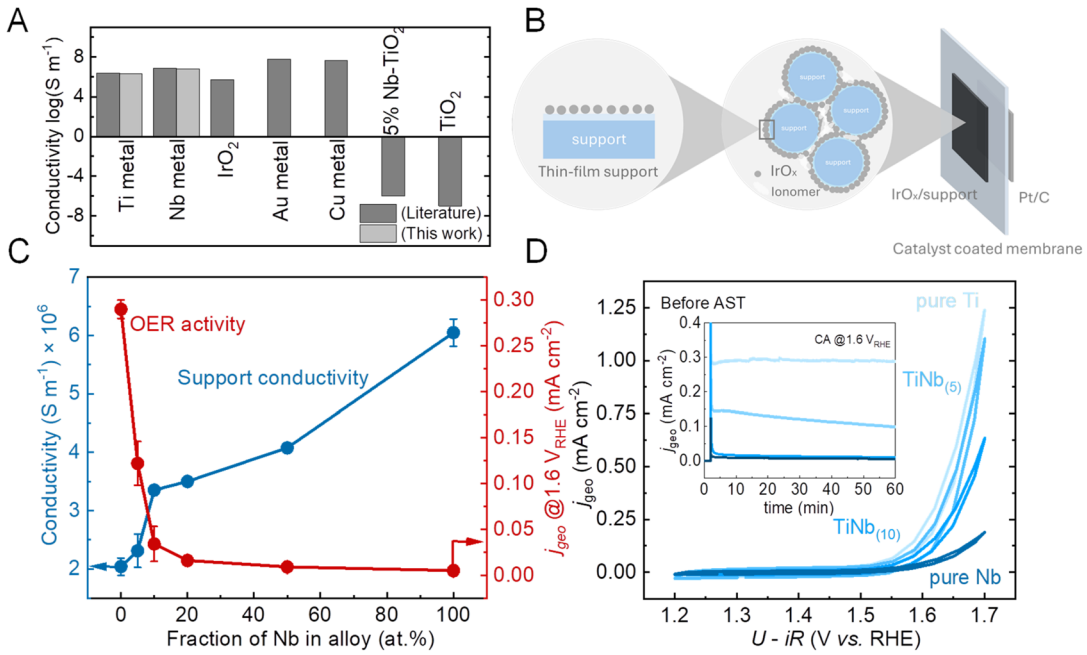

Fig. 1 (A) Conductivity of different materials from this work compared with literature data. Ti, Nb, Au and Cu metals are from ref. 50, IrO_2 thin film is from ref. 51 and Nb doped TiO_2 and pure TiO_2 references are from ref. 39. (B) Schematic of a catalyst coated membrane (CCM) consisting of a Nafion membrane with catalyst layers deposited on both sides. The zoom-in of the anode side illustrates IrO_x particles supported on support particles. A further magnified view highlights the thin-film support system in this study to decouple the electrical conductivity contribution from IrO_x. (C) Conductivity of the Ti–Nb thin film supports with varied Nb content and the corresponding activities of the supported IrO_x. Conductivity of supports was tested by van der Pauw four-point probe on glass substrates and activity of Ti–Nb supported IrO_x demonstrated by averaging chronoamperometry (CA) results. (D) Initial activity of Ti–Nb supported IrO_x on glassy carbon disc substrates. Cyclic voltammetry (CV) was collected using RDE (100 mV s^{-1}, 0.1 M $HClO_4$, 1600 rpm) and CA (inset) was collected using RDE at 1.6 V_{RHE} for 60 min in 0.1 M $HClO_4$.

spectrometry (ICP-MS)) to unravel the relationships between film thickness and atomic structure for the *in situ* oxide passivation layers that form on the support. Independent of film composition, we find a ~10 nm oxide passivation layer forms on the surface. Interestingly, we find that in the Ti–Nb alloy films, the surface oxide changes from the anatase phase (for pure Ti) to rutile (for Ti with 50 at% Nb), which exhibits increased resistance and reduced OER kinetics despite the bulk conductivity of Ti–Nb alloys increasing with Nb content. Our study thus highlights the role of the surface oxide phases formed under OER conditions in controlling the conductivity of support materials for Ir-based catalysts in PEM electrolysers.

Experimental

Sample preparation

Ti–Nb thin films with different Nb to Ti ratio were prepared by sputter deposition (AJA, ACT O8-17347, Size B, Reversion 2) on glassy carbon discs (SIGRADUR G discs, diameter 5.0 (±0.05) mm, height 4.0 mm) for electrochemical measurements and on silicon wafers and glass for additional characterisations. Samples prepared are denoted as pure Ti, $TiNb_{(5)}$ $TiNb_{(10)}$ $TiNb_{(20)}$ $TiNb_{(50)}$ pure Nb with the numbers referring to the Nb atomic percentage in the sample. The glassy carbon substrates were polished with diamond paste (0.25 μm) and cleaned by sonicating in IPA and Millipore 18.2 MΩ cm ultra-pure water for 10 min each. 100 nm of the Ti–Nb thin films were sputtered from a Ti target (AJA, 99.995%) and a Nb target (AJA, 99.95%) at a process pressure of 3 mTorr under Ar (BOC, 99.9999%) with powers stated in Table S1. IrO_x synthesised from a hydrothermal method adopted from the literature[41] was then drop-cast onto these thin films after sonication for 10 min. The ink was prepared in 70 : 30 ultra-pure water : IPA, with 10 μL of 5 wt% Nafion added to each 1 mL of the ink. 10 μL of the ink was drop-cast onto the sample coated glassy carbon discs to achieve an iridium loading of 10 μg cm^{-2}.

Electrochemical measurements

The electrochemical measurements were conducted using a Pine instrument Company E6-series ChangeDisk rotating disc electrode (RDE) assembly and affixed to a WaveVortex electrode rotator with a jacket three electrode cell containing a reference electrode (a reversible hydrogen electrode (RHE) immersed in an electrolyte filled Luggin capillary) and a counter electrode (Pt mesh). The OER activities of supported IrO_x were recorded using a Biologic SP-300 potentiostat and EC-Lab software with the rotation speed of 1600 rpm at room temperature. The three-electrode cell was filled with fresh electrolyte, 0.1 M $HClO_4$ (pH ~ 1.1, diluted perchloric acid, TraceSELECT™ Ultra, 67 to 72%, Honeywell Fluka™ $HClO_4$ stock). Chronoamperometry (CA) was firstly carried out by holding the potential at 1.6 V_{RHE} for 1 hour. The current was recorded after being stabilised for activity comparison. The accelerated stress test (AST) was conducted subsequently by cycling in a potential window from 1.2 V_{RHE} to 1.7 V_{RHE} for 3000 cycles at 100 mV s^{-1}. The workflow is shown in Fig. S1. Electrochemical impedance spectroscopy (EIS) was carried out over the range of 200 kHz to 100 mHz under a DC potential of 1.6 V_{RHE} with the sinus amplitude of 10 mV. All data were corrected for ohmic losses manually.

Four-point probe conductivity tests

The resistivity (ρ, Ω cm) of each Ti–Nb thin film grown on plain glass was measured using a four-point probe:

$$\rho = \frac{\pi}{\ln 2}\left(\frac{V}{I}\right)t \quad (1)$$

where t (cm) is the thickness of the thin film. This equation is applicable when the sample thickness is less than half the probe spacing (1 mm).[42] The voltage and current were recorded using a multi-metre (Agilent 34401A).

Inductively coupled plasma mass spectrometry (ICP-MS)

ICP-MS (ICP-QQQ, Agilent 8900 triple quadrupole) was used, with helium as the collision gas for Ir and Nb and oxygen as the reactive gas for Ti, to determine the concentration of the dissolved Ti, Nb and Ir from each AST. The instrument was configured with an Agilent SPS 4 open-bed autosampler, Ultra High Matrix Introduction (UHMI), quartz spray chamber, quartz torch and a nickel sampling cone. The standards and the samples were run in triplicate using single quad scan mode. The instrument was tuned using a standard tuning mix. A 10 mL aliquot from the 130 mL total of the electrolyte was taken from the electrochemical testing cell after each AST. Each sample was analysed in triplicate using ICP-MS, and the reported values represent the mean of the three measurements. The variation between replicates was less than 5 CPS. The machine was calibrated against standards for Ir ($IrCl_3$ in HCl 7% 1000 mg L^{-1} Ir CertiPUR®), Ti (TraceCERT®, 1 g L^{-1} Ti in nitric acid (nominal concentration)) and Nb (TraceCERT®, 1 g L^{-1} Nb in 0.1 M $HClO_4$ (nominal concentration)) at 0, 0.1, 0.5, 1, 10, 50, 100, 200 ppb, with calibration curve showing a coefficient of determination R^2 above 0.999.

FIB-TEM images

Cross-sectional lamellae suitable for transmission electron microscopy (TEM) analysis were prepared *via* focused ion beam (FIB) milling. TEM data were collected using an FEI Tecnai Osiris TEM, which features a high-brightness Schottky X-FEG source and a Super-EDX system with four silicon drift detectors. Scanning/transmission electron microscopy (S/TEM) images were captured at an acceleration voltage of 200 kV. Electron Energy Loss Spectroscopy (EELS) data was acquired using Gatan GMS on an Enfinium spectrometer in dual-EELS mode.

X-ray photoelectron spectroscopy (XPS) and near-edge X-ray absorption fine structure spectroscopy (NEXAFS)

The chemical states of Ti, Nb and Ir were analysed by a Thermo Scientific K-Alpha + X-ray photoelectron spectrometer with monochromatic Al Kα X-ray radiation. Binding energies were adjusted to adventitious graphitic C (284.8 eV) and the

deconvolution was conducted using CasaXPS, fitting information is shown in the SI. The XPS spectrum of the as-synthesised IrO_x suggests mixed oxidation states, with IrO_x comprising mainly Ir^{4+} and ~20% Ir^{3+} (Fig. S2).

NEXAFS spectroscopy was conducted at the Versatile Soft X-ray (VerSoX) beamline B07-B of Diamond Light Source, UK. 100 nm of Ti–Nb as-deposited and cycled in the electrolyte with silicon wafers as the substrate were affixed to a multisampling holder (Omicron plate) using copper-supported carbon tape. In order to exclude any oxygen contribution from IrO_x, the samples were scanned from 1.2–1.7 V_{RHE} for 3000 cycles without IrO_x. To ensure proper electrical grounding, copper tape was employed to connect the sample surface to the holder. The photon energy resolution was set at 50 meV, with scan ranges spanning 520 eV to 570 eV for the O K-edge and 450 eV to 475 eV for the Ti L-edge. Spectra were acquired in total electron yield (TEY) mode at room temperature, under a helium atmosphere at 1 mbar pressure to mitigate sample charging.

Results and discussion

TiO_2 is stable under the acidic and corrosive operational conditions needed for the OER in a PEM electrolyser.[43] However, its insulating nature requires severely high amount of IrO_x to sustain the conductivity and activity of the catalyst layer. For instance, the Ir content in commercially available supported IrO_x, Umicore IrO_x/TiO_2, is 75 wt%. As shown in Fig. 1A, although Nb-doping improved the conductivity of TiO_2 compared to the undoped material,[38,44,45] the conductivity of Nb-doped TiO_2 remains more than 10 orders of magnitude lower than IrO_2 which has a similar conductivity to most metals. Much less well studied is the role of Nb doping in metallic Ti supports. To investigate the influence Nb alloying in Ti thin films on the OER activity of supported IrO_x, films with 0, 5, 10, 20, 50 and 100 at% Nb (denoted as pure Ti, $TiNb_{(5)}$, $TiNb_{(10)}$, $TiNb_{(20)}$, $TiNb_{(50)}$ and pure Nb, respectively) were prepared on various substrates (glassy carbon discs for electrochemistry measurement, silicon wafers and glass for characterisation) using a sputter deposition method (Fig. S3). X-ray photoelectron spectroscopy (XPS) revealed the atomic ratio of Nb to Ti in the surfaces of the films are in good agreement with the nominal bulk compositions, based on the synthesis conditions (Table S1). Nb metal (6.9×10^6 S m^{-1}) possesses higher conductivity than Ti metal (2.4×10^6 S m^{-1}) at room temperature[46] (Fig. 1A). In agreement with the literature, the conductivity of the pure Nb thin film was nearly 3 times higher than the pure Ti thin film with the conductivities of these mixed metals increasing with Nb content in a near linear fashion (Fig. 1C).

To evaluate the suitability of the support for the OER conditions, a combined approach was taken, where a rotating disc electrode (RDE) set-up was used to study the activity and stability of our electrocatalysts in an acidic electrolyte environment (0.1 M $HClO_4$, pH ~ 1.1) and inductively coupled plasma mass spectrometry (ICP-MS) was used to detect any dissolution of either the IrO_x catalyst or Ti and Nb in the support into the electrolyte. Scanning electron microscopy (SEM) images were taken of bare $TiNb_{(x)}$ samples and the samples loaded with IrO_x, revealing no significant difference in the film morphology and the IrO_x distribution on the supports (Fig. S4). We have also included the cyclic voltammograms (Fig. S5) of two independently prepared and IrO_x loaded samples which verify the reproducibility of our methodology. The conductivity of the supports was tested by van der Pauw four-point probe method on glass substrates and the activity of the Ti–Nb supported IrO_x was demonstrated by averaging chronoamperometry (CA) results and holding the potential at 1.6 V_{RHE} for 1 h.

As shown in Fig. 1C, the geometric IrO_x activity was found to decrease with increasing Nb content; a reverse trend to what was seen for the support conductivity (blue points) measured by our four-point probe. The IrO_x supported on pure Ti metal film exhibited the highest OER activity (~0.27 mA cm^{-2} CA at 1.6 V_{RHE}), which was assessed by holding the potential at 1.6 V_{RHE} for 1 h (Fig. 1D, inset). To benchmark the activity of supported IrO_x in this study, we have also included an activity test on a polycrystalline gold (Au) disk (Fig. S6) which has a comparable mass-normalised activity with recent published papers using rotating disk electrode (Fig. S7 and Table S2). The current density is nearly 10 times higher on the Au disk than when supported on any of the Ti–Nb alloys at 1.6 V_{RHE} owing to the oxide passivation layer formed on Ti–Nb alloy supports. The activity of all supported IrO_x saw some decay during CA, which is likely because of the formation of oxidation layer between the support and IrO_x. To assess the longer-term stability of the support materials, accelerated stress tests (AST) were carried out by scanning through 1.2–1.7 V_{RHE} for 3000 cycles at a scan rate of 100 mV s^{-1} (*i.e.* an ~8 h test) using a stability test protocol established in previous work.[47,48] The cyclic voltammograms (CVs) from the first and last cycles are shown in Fig. 1D and 2A, respectively. Only the pure Ti supported iridium sample was able to maintain the OER activity to the end of this stability test, with all other Nb-containing samples as a result showing near zero OER activity by the final cycle (Fig. 2A).

Interestingly, the pure Ti support showed a higher activity after the AST than on initial testing, with the geometric current density doubling from ~1.25 mA cm^{-2} to ~2.5 mA cm^{-2} at 1.7 V_{RHE} after 3000 cycles. This activity gain is not accompanied by a measurable increase in non-faradaic double-layer capacitance (Fig. S8), indicating that the number of electrochemically accessible IrO_x sites (or geometric roughness) does not significantly increase. In contrast, electrochemical impedance spectroscopy (EIS) (Fig. S8) reveals a decrease in the charge-transfer resistance after the AST, suggesting improved per-site charge-transfer kinetics at the IrO_x/TiO_x interface. These observations point to an electronic and structural evolution of the IrO_x/TiO_x system rather than a simple increase in surface area. In our system, which involves both IrO_x and a Ti-based support, the observed activation after AST could therefore arise from an improved support conductivity/interfacial electronic coupling. While our current dataset does not allow us to unambiguously determine the origin of this phenomenon, the absence of capacitance growth together with the reduced charge-transfer resistance strongly suggests that the activation is electronic/structural in nature rather than due to increased roughness or IrO_x loading.

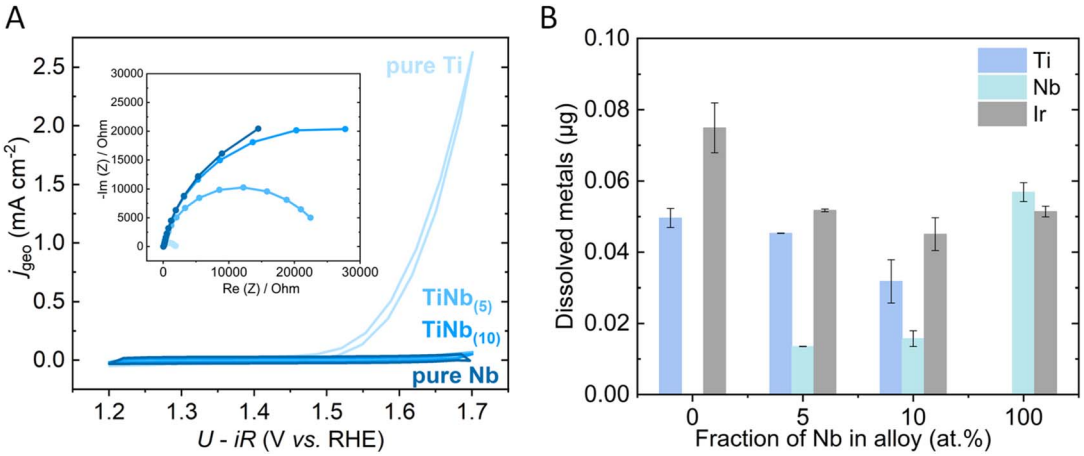

Fig. 2 (A) Geometric OER activity of IrO_x on the series of Ti–Nb supports and (inset) the EIS at 1.6 V_{RHE} after the AST (RDE, 1.2–1.7 V_{RHE}, 100 mV s^{-1}, 3000 cycles, 0.1 M $HClO_4$, 1600 rpm). (B) The degree of Ti, Nb and Ir dissolution (µg) in the electrolyte (130 mL of 0.1 M $HClO_4$) after the AST. Error bars are the range from two independent AST experiments, values are the average.

To investigate if the activity decay seen for the Nb alloyed Ti thin film supports was due to dissolution of Ir, ICP-MS was conducted to examine the degree of dissolution of metals (Ti, Nb and Ir) in the electrolyte after the AST (Fig. 2B). The amount of Ir dissolution presented no clear trend, irrespective of Ti–Nb supports used, with the degree of dissolved Ir being less than 3% of the total Ir loaded on each support. This showed that the activity loss does not come primarily from the dissolution of Ir. Rather, we attribute this to the oxidation of the surface of the support resulting in a barrier to charge transport. The ICP-MS measurements indicated that only around 0.5 nm of the 100 nm thick support film was dissolved during the AST, which confirms the robustness of the passivation layer (calculation provided in SI Table S3). XPS was also conducted on the Ti–Nb alloy supports after the AST with Nb : Ti ratio found to increase slightly by 1–2 at%. This can be attributed to a higher dissolution rate of Ti compared to Nb (consistent with what is measured by ICP-MS, see Table S3). To enable comparison of dissolution behaviour across samples with different activities, we integrated the charge passed during the AST and converted it into an apparent oxygen turnover, assuming 100% faradaic efficiency (Fig. S9). The total dissolved metal species in mol are shown in Fig. S10a, and the corresponding stability numbers (*S*-numbers) for Ir, Ti and Nb are presented in Fig. S10b. While the *S*-number is commonly used to assess the stability of OER electrocatalysts, its application to support materials is less direct, as the support influences activity through interfacial effects rather than participating in oxygen evolution. Nevertheless, a clear support-dependent trend is observed: Ir exhibits higher *S*-numbers than Ti and Nb, and all *S*-numbers decrease with increasing Nb content, indicating reduced activity and stability upon Nb alloying. The AST protocol used here is based on dynamic potential cycling, whereas the *S*-numbers reported in the literature are usually done with steady state protocols.[49,50] The calculated *S*-numbers therefore are protocol-dependent, and these values are used solely for relative comparison within this study. Importantly, the observed trends support our conclusion that the structure of the electrochemically formed surface oxide, rather than bulk conductivity alone, governs both activity and stability. The same AST protocol was also applied to Au supported IrO_x. As discussed above, IrO_x supported on Au exhibits significantly higher activity than on Ti-based supports under identical conditions (Fig. S11a). This can be attributed to the absence of a passivating oxide layer and the resulting lower interfacial resistance at the IrO_x/Au interface as reflected by the high frequency resistance (Fig. S11b). Despite the higher activity, Au-supported IrO_x also shows increased Ir dissolution, leading to *S*-number that is comparable to that of Ti-supported IrO_x (Fig. S12a). This suggests that the intrinsic stability of Ir active sites is similar in both systems. Notably, the difference in activity between Au- and Ti-supported IrO_x cannot be accounted for by *iR* correction alone. As shown in the inset of Fig. S11a, the non-faradaic capacitance of Au-supported IrO_x is much higher than that of Ti-supported IrO_x at the same Ir loading (10 µg cm^{-2}), indicating a larger electrochemically active surface area. The difference in performance of Ti supported IrO_x and Au supported IrO_x can be largely eliminated by normalising the current density with the capacitance (Fig. S12b). We therefore attribute the lower activity on Ti to the presence of a passivation layer, which not only introduces an additional charge-transfer barrier but also limits the accessibility of active sites.

The EIS spectra at 1.6 V_{RHE} after the AST (Fig. 2A, inset) also support our assertion that a more insulating oxide layer was formed on Nb alloyed Ti compared with pure Ti, showing an increase in charge transfer resistance with Nb alloying. The pure Nb support exhibited the lowest Ir activity and the highest charge transfer resistance, which suggests the formation of insulating Nb_2O_5.[45,51] Catalyst anchoring could, in principle, contribute to the activity loss observed on the Nb-doped samples. However, in our system both the support metals and Ir exhibit negligible concentration in the electrolyte under the applied OER conditions. We therefore consider detachment of the catalyst during support oxidation unlikely and exclude it as the origin of the observed activity loss.

XPS analysis enables comparison of the surface oxidation behaviour for the as-synthesised and post-AST supports, to better understand the passivation behaviour that occurs during the AST. The XPS spectra of Ti 2p and Nb 3d of pure Ti, $TiNb_{(50)}$ and pure Nb before and after the AST are shown in Fig. 3A (with fitting information provided in the SI Tables S4 and S5). Before the AST, the $TiNb_{(50)}$ film showed metal, suboxide and oxide species: Ti^0, Ti^{2+}, Ti^{3+}, Ti^{4+} and Nb^0, Nb^{2+}, Nb^{4+}, Nb^{5+}.[52,53] After the AST, the $TiNb_{(50)}$ film primarily showed fully oxidised Ti^{4+} and Nb^{5+} states, indicating a thickening of the surface oxide layer during electrochemical cycling. On the pure Ti thin film surface, both before and after the AST, the predominant specie was Ti^{4+}, consistent with the presence of the expected native oxide passivation layer on this metal. For the pure Nb film, the Nb metal or suboxide species present on the as-prepared films disappeared after AST, consistent with the formation of thicker surface oxide layer during cycling. It is interesting, that the amount of metal detected for the Ti–Nb alloy thin film is greater than for the pure Nb or Ti suggesting that rather than adopting an intermediate thickness, alloying reduces the thickness of the native oxide phase compared to the pure metals. The conductivity of the oxidised Ti–Nb supports shows no change when measured with a four-point probe, which we attribute to the measurement being dominated by the bulk conductivity where the contribution of the surface oxide is negligible.

To investigate the local structure of the surface oxides, near edge X-ray absorption fine structure spectroscopy (NEXAFS) was performed at the Diamond Light Source synchrotron facility on both pure Ti and $TiNb_{(50)}$ samples before and after 3000 cycles of their AST. The total electron yield (TEY) of the O K edge examined between 530 and 550 eV is shown in Fig. 3B. The Ti–Nb alloy possessed some features in the O K edge spectra indicating surface oxidation as the TEY detection mode in NEXAFS is highly surface-sensitive, with a probe depth typically ranging from 1 to 5 nanometres.[54] This included peak formation at ~533.5 and 537 eV. Interestingly, the ~533.5 eV peak was more intense in the $TiNb_{(50)}$ sample, which was more indicative of the rutile oxide structure being formed, whereas the ~537 eV peak was more intense in the pure Ti sample, which was more indicative of the anatase oxide structure being formed. Both anatase and rutile are intrinsic n-type semiconductors due to the oxygen vacancies that form within the crystal lattice.[55] These oxygen vacancies can act as electron donors serving as the primary charge carriers. The electron conduction of TiO_2 comes from the formation and movement of polarons, which comprises an electron coupled with a local distortion of the crystal lattice.[56] The electrons hop from one lattice to another when being activated by heat or electric field and the number and the size of polarons in the materials determine the intrinsic conductivity. Anatase TiO_2 is widely reported to have a higher propensity to form polarons than rutile TiO_2, which results in more delocalised electrons in the anatase form and higher electronic conductivity.[40,57] Therefore, based on these XAS results of samples examined after AST, we suggest that when alloyed with Nb, Ti tends to be oxidised to a more thermodynamically stable but more insulating rutile-like structure whereas the metastable anatase-like oxide forms on the undoped Ti metal surface, and thus, charge transfer from the support to the IrO_x catalyst is more hampered in Nb-containing Ti samples. To address whether the formation of the anatase phase on pure Ti is driven by electrochemical oxidation or directly linked to OER turnover, a pure Ti sample was subjected

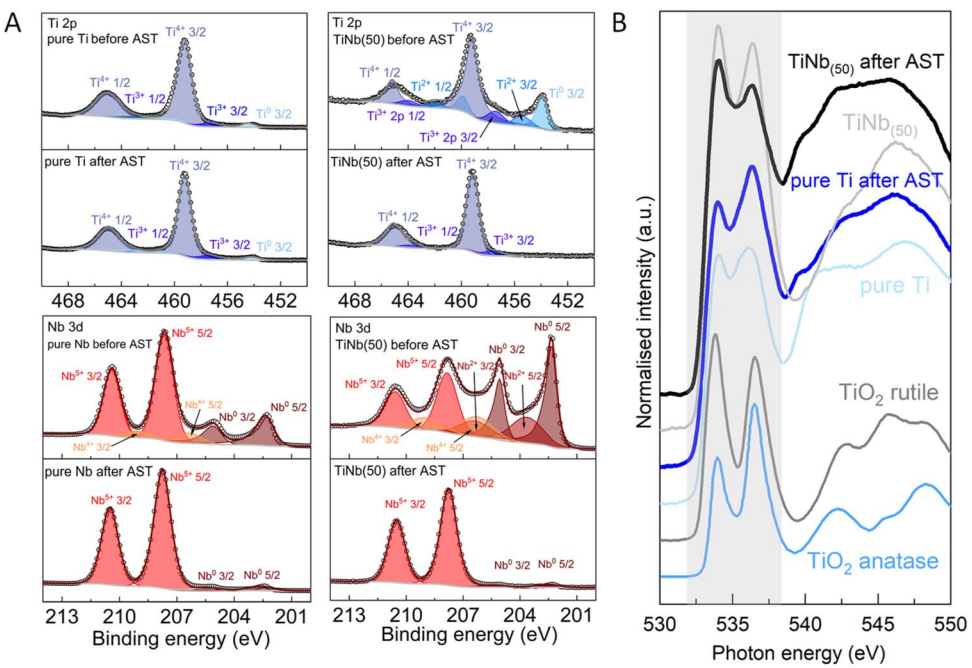

Fig. 3 (A) XPS of the Ti 2p and Nb 3d binding energy regions in pure Ti, $TiNb_{(50)}$ and pure Nb thin films before and after their AST (RDE, 1.2–1.7 V_{RHE}, 100 mV s^{-1}, 3000 cycles, 0.1 M $HClO_4$, 1600 rpm). (B) NEXAFS of the O K-edge of pure Ti and $TiNb_{(50)}$ before and after their AST.

to the same AST protocol in the absence of IrO_x (NEXAFS shown in Fig. S13). For this sample, the peak at ~537 eV is more intense than that at ~533.5 eV, consistent with the formation of an anatase-like TiO_2 phase, like the behaviour observed for Ti samples tested with IrO_x. This indicates that the anatase phase formation is primarily driven by electrochemical oxidation of the Ti surface under anodic conditions and does not require OER turnover at the catalyst.

Focused ion beam (FIB) milling was used to prepare cross sectional specimens of the surfaces of the thin films and enable transmission electron microscopy (TEM) investigation of the oxide layers on the $TiNb_{(50)}$ and pure Ti thin films after their AST. Electron energy loss spectroscopy (EELS) elemental analysis was performed to image the thickness of the oxide layers, showing that post-AST both samples had surface oxides around 10 nm thick (Fig. 4A and C). High resolution TEM imaging was also performed for these samples and fast Fourier transforms (FFTs) of the high-resolution images compared to simulated electron diffraction patterns (Fig. S14–S16). For the pure Ti sample, an anatase phase oxide ($I4_1/amd$ space group) was observed at the surface whereas the bulk remained metallic (Fig. 4B). In contrast, the oxide formed on the Nb alloyed Ti, $TiNb_{(50)}$ sample, exhibited a rutile structure ($P4_2/mnm$ space group) (Fig. 4D). These results were in agreement with our XAS studies, where surface oxidation was seen, with a greater tendency to form the rutile oxide phase on the Ti–Nb alloy ($TiNb_{(50)}$) and the anatase oxide phase on the pure Ti support.

Our XAS and TEM results showed the formation of a ~10 nm oxide layer on the surface of Ti–Nb alloy supports after the AST (1.2–1.7 V_{RHE}, 3000 cycles) while the native oxide on bare Ti in the literature has been reported to be 5–8 nm.[58,59] Yet despite the similar oxide layer thickness after alloying, the through-plane conductivity of the support and the OER activities show significant differences. This suggests that the structure of the oxide layer formed on the surface is important as well as the thickness of this layer for dictating the conductivity between IrO_x and the support, and consequently activity of the supported catalyst. The finding provides insights that are relevant to Ti-based materials more broadly, particularly for Ti-based porous transport layers in PEM water electrolysers. While Nb alloying improves the bulk conductivity of Ti, it also alters the structure of the surface oxide, promoting the formation of a more insulating rutile-type TiO_2, which plays a more dominant role in governing catalytic activity in our system. However, these findings from a model system to device level operation require consideration of additional factors such as porosity, gas transport and mechanical properties.[60]

Our findings indicate that the passivation layer on Ti is unlikely to thicken or impede charge transfer to IrO_x under the OER conditions within the potential range of 1.2–1.7 V_{RHE}. It has been reported that Ir nanoparticles will stabilise and reduce the oxide layer growth on Ti oxynitride supports by 10 times.[30] Based on these findings and given the much higher conductivity and lower fabrication cost of Ti metal, our study highlights the potential of using pure Ti metal as a support for IrO_x with good interfacial contact and coverage to suppress passivation layer formation and preserve catalytic activity. It is important to note that the configuration adopted in this study, in which an IrO_x

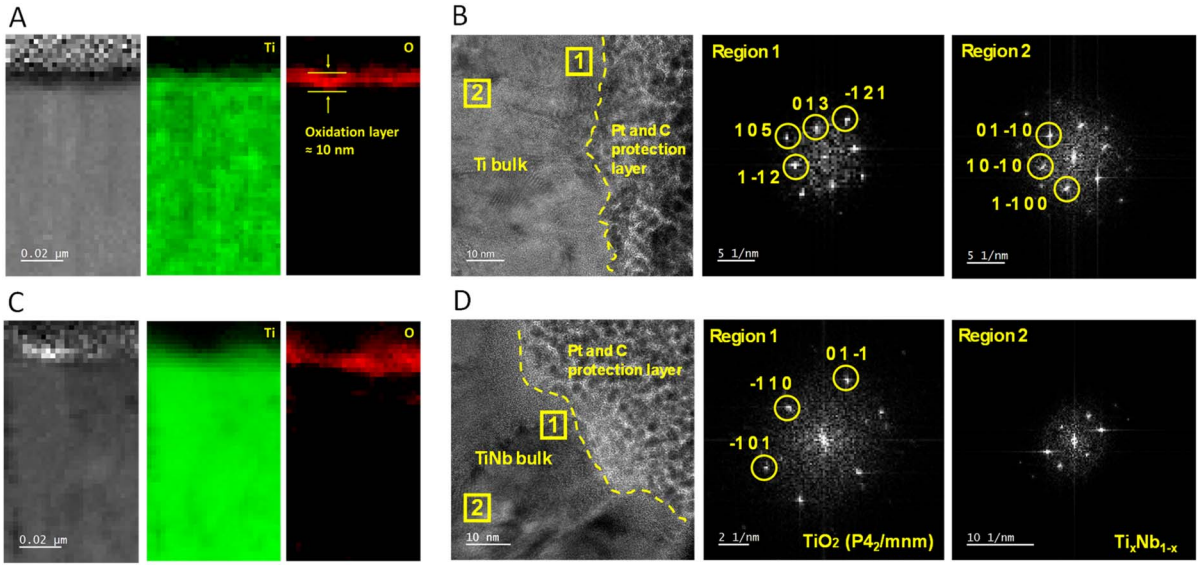

Fig. 4 Cross-sectional scanning TEM (STEM) and EELS characterisation of FIB milled cross sectional samples at the surface for the pure Ti and $TiNb_{(50)}$ supports after the AST tested with IrO_x (RDE, 1.2–1.7 V_{RHE}, 100 mV s^{-1}, 3000 cycles, 0.1 M $HClO_4$, 1600 rpm). (A) Left image is a bright-field TEM cross section image, middle and right are TEM-EELS elemental mapping of Ti and O, respectively. (B) Left is an STEM cross section image of pure Ti after the AST, the Pt and C coating was applied to the surface to protect it during FIB. Middle and right are the FFT of the high resolution images for of region 1 (less than 10 nm from the surface) and region 2 (50 nm below the surface), respectively. (C) Left is a bright field TEM cross section image, middle and right are TEM-EELS elemental mapping of Ti and O, respectively. (D) Left is an STEM cross section image of $TiNb_{(50)}$ after the AST. Middle and right are the FFTs of high resolution images for of region 1 (10 nm from the surface) and region 2 (50 nm from the surface), respectively. The FFTs are indexed to the crystal structures indicated bottom right on each pattern.

catalyst ink is drop-cast onto a planar support, is designed to isolate the effects of support passivation under well-defined conditions. This model system is therefore not directly analogous to conventional high-surface-area catalyst–support systems, where the catalyst is grown or strongly anchored onto the support.[20,61,62]

Conclusions

In summary, this work demonstrates a rapid and well-defined screening platform to elucidate support-related effects on the activity and stability of IrO_x oxygen evolution electrocatalysts. Using a series of Ti–Nb alloy thin films, we find that increasing support conductivity through Nb alloying does not lead to enhanced catalytic performance. Instead, the OER activity of IrO_x decreases with increasing Nb content despite higher substrate conductivity. Combing characterisation techniques on pristine and post-AST (1.2–1.7 V_{RHE}, 3000 cycles, 100 mV s^{-1}) samples using XAS, HRTEM and XPS, we identify this behaviour is driven by the *in situ* formation of an interfacial oxide: on pure Ti, an anatase-type oxide passivation layer (~10 nm) remains stable during AST (1.2–1.7 V_{RHE}, 3000 cycles, 100 mV s^{-1}) and does not impede charge transfer, whereas Nb containing alloys formed a more resistive rutile-type oxide that increases interfacial resistance and reduces activity. These results show that improving bulk conductivity of the support alone is insufficient; the conductivity and structure of oxides formed *operando* play a decisive role in governing charge transfer and catalytic performance. Importantly, our results show that Ti is a promising non-precious support for IrO_x in PEM water electrolysers, provided the initial passivation barrier is mitigated. We therefore propose that future efforts should prioritise interface engineering (*e.g.*, compact/adhesive interlayers and anchoring strategies) to lower interfacial resistance and enhance electron extraction without promoting further oxide growth. While the present study is intentionally conducted using planar thin-film model systems, the mechanistic insights obtained here provide clear design principles that can be translated to high-surface-area catalyst–support systems aimed at reducing iridium loading in practical PEM water electrolysers.

Author contributions

G. Y. synthesised the samples, performed electrochemical measurements, conducted characterisations (XPS, XAS and ICP-MS) and drafted the original manuscript. W. H. conducted FIB preparation and acquired TEM images. Y. W. and C. L. assisted with NEXAFS experiments and data analysis. Y. Z. obtained SEM images. S. K., P. F. E., and G. H. contributed to NEXAFS measurements. P. N. and G. S. assisted with thin-film deposition and data interpretation. T. F. supported ICP-MS analysis and troubleshooting. M. T., S. J. H., and C. D. assisted with microscopy and data discussion. A. K. and R. R. R. supervised the project and contributed to manuscript review and editing. All authors have read and approved the final version of the manuscript.

Conflicts of interest

There are no conflicts to declare.

Data availability

The data supporting this article have been included as part of the supplementary information (SI). Supplementary information is available. See DOI: https://doi.org/10.1039/d5ta08384b.

Acknowledgements

G. Y. thanks Imperial College London for the President's PhD scholarship. This project was supported by the Royal Academy of Engineering under the Research Fellowship program (R. R. R.). A. K. thanks the EPSRC for a Programme Grant (EP/W017075/1) and the Royal Society for an Equipment Grant (RSG\R1\180434). W. H. acknowledges the support of the Wolfson Electron Microscopy Suite and use of the FEI Osiris G2 200. We acknowledge Diamond Light Source for time on Beamline B07 under Proposal SI37550 and greatly appreciate the help from Ms Youli Yu, Mr Sid Halder and Dr Norton West with the synchrotron measurements. The authors would like to thank Imperial College London Agilent Measurement Suite for use of the ICP 8900 instrument. The authors would like to thank the Royce Industrial Collaborator Programme (grant number MCAP029 and ICP349).

Notes and references

1 International Energy Agency, *The Breakthrough Agenda Report 2023*, 2023.
2 O. Schmidt, A. Gambhir, I. Staffell, A. Hawkes, J. Nelson and S. Few, *Int. J. Hydrogen Energy*, 2017, **42**, 30470–30492.
3 M. A. Hubert, L. A. King and T. F. Jaramillo, *ACS Energy Lett.*, 2022, **7**, 17–23.
4 M. Bernt, A. Siebel and H. A. Gasteiger, *J. Electrochem. Soc.*, 2018, **165**, F305–F314.
5 M. Clapp, C. M. Zalitis and M. Ryan, *Catal. Today*, 2023, **420**, 114140.
6 U.S. Department of Energy, *Technical Targets for Proton Exchange Membrane Electrolysis*, 2023.
7 M. Bernt, A. Hartig-Weiß, M. F. Tovini, H. A. El-Sayed, C. Schramm, J. Schröter, C. Gebauer and H. A. Gasteiger, *Chem. Ing. Tech.*, 2020, **92**, 31–39.
8 C. Rozain, E. Mayousse, N. Guillet and P. Millet, *Appl. Catal., B*, 2016, **182**, 153–160.
9 C. Daiane Ferreira Da Silva, F. Claudel, V. Martin, R. Chattot, S. Abbou, K. Kumar, I. Jiménez-Morales, S. Cavaliere, D. Jones, J. Rozière, L. Solà-Hernandez, C. Beauger, M. Faustini, J. Peron, B. Gilles, T. Encinas, L. Piccolo, F. H. Barros De Lima, L. Dubau and F. Maillard, *ACS Catal.*, 2021, **11**, 4107–4116.
10 Y. N. Regmi, E. Tzanetopoulos, G. Zeng, X. Peng, D. I. Kushner, T. A. Kistler, L. A. King and N. Danilovic, *ACS Catal.*, 2020, **10**, 13125–13135.

11 C. Rozain, E. Mayousse, N. Guillet and P. Millet, *Appl. Catal., B*, 2016, **182**, 123–131.
12 R. A. Krivina, M. Zlatar, T. N. Stovall, G. A. Lindquist, D. Escalera-López, A. K. Cook, J. E. Hutchison, S. Cherevko and S. W. Boettcher, *ACS Catal.*, 2023, **13**, 902–915.
13 H. P. Tran, H. N. Nong, M. Zlatar, A. Yoon, U. Hejral, M. Rüscher, J. Timoshenko, S. Selve, D. Berger, M. Kroschel, M. Klingenhof, B. Paul, S. Möhle, K. N. Nagi Nasralla, D. Escalera-López, A. Bergmann, S. Cherevko, B. R. Cuenya and P. Strasser, *J. Am. Chem. Soc.*, 2024, **146**, 31444–31455.
14 Y. N. Regmi, E. Tzanetopoulos, G. Zeng, X. Peng, D. I. Kushner, T. A. Kistler, L. A. King and N. Danilovic, *ACS Catal.*, 2020, **10**, 13125–13135.
15 H. Ohno, S. Nohara, K. Kakinuma, M. Uchida and H. Uchida, *Catalysts*, 2019, **9**, 74.
16 G. C. da Silva, S. I. Venturini, S. Zhang, M. Löffler, C. Scheu, K. J. J. Mayrhofer, E. A. Ticianelli and S. Cherevko, *ChemElectroChem*, 2020, **7**, 2330–2339.
17 F. Karimi and B. A. Peppley, *Electrochim. Acta*, 2017, **246**, 654–670.
18 A. Hartig-Weiss, M. Miller, H. Beyer, A. Schmitt, A. Siebel, A. T. S. Freiberg, H. A. Gasteiger and H. A. El-Sayed, *ACS Appl. Nano Mater.*, 2020, **3**, 2185–2196.
19 H. S. Oh, H. N. Nong and P. Strasser, *Adv. Funct. Mater.*, 2015, **25**, 1074–1081.
20 A. Bornet, R. Pittkowski, T. M. Nielsen, E. Berner, A. Maletzko, J. Schröder, J. Quinson, J. Melke, K. M. Ø. Jensen and M. Arenz, *ACS Catal.*, 2023, **13**, 7568–7577.
21 M. Kost, M. Kornherr, P. Zehetmaier, H. Illner, D. S. Jeon, H. Gasteiger, M. Döblinger, D. Fattakhova-Rohlfing and T. Bein, *Small*, 2024, **20**, 2404118.
22 E. Oakton, D. Lebedev, M. Povia, D. F. Abbott, E. Fabbri, A. Fedorov, M. Nachtegaal, C. Copéret and T. J. Schmidt, *ACS Catal.*, 2017, **7**, 2346–2352.
23 R. V. Genova-Koleva, F. Alcaide, G. Álvarez, P. L. Cabot, H. J. Grande, M. V. Martínez-Huerta and O. Miguel, *J. Energy Chem.*, 2019, **34**, 227–239.
24 O. Kasian, T. Li, A. M. Mingers, K. Schweinar, A. Savan, A. Ludwig and K. Mayrhofer, *J. Phys.: Energy*, 2021, **3**, 034006.
25 R. Muntean, D. T. Pascal, U. Rost, L. Holtkotte, J. Näther, F. Köster, M. Underberg, T. Hülser and M. Brodmann, *Top. Catal.*, 2019, **62**, 429–438.
26 Y. Qin, Y. Wang, R. Wen, L. Wang, M. Dou and F. Wang, *ACS Catal.*, 2024, **14**, 13915–13926.
27 S. Siracusano, V. Baglio, C. D'Urso, V. Antonucci and A. S. Aricò, *Electrochim. Acta*, 2009, **54**, 6292–6299.
28 G. Li, K. Li, L. Yang, J. Chang, R. Ma, Z. Wu, J. Ge, C. Liu and W. Xing, *ACS Appl. Mater. Interfaces*, 2018, **10**, 38117–38124.
29 L. Suhadolnik, M. Bele, M. Čekada, P. Jovanovič, N. Maselj, A. Lončar, G. Dražić, M. Šala, N. Hodnik, J. Kovač, T. Montini, M. Melchionna and P. Fornasiero, *Chem. Mater.*, 2023, **35**, 2612–2623.
30 G. Koderman Podborsek, L. Suhadolnik, A. Loncar, M. Bele, A. Hrnjic, Z. Marinko, J. Kovac, A. Kokalj, L. Gasparic, A. K. Surca, A. R. Kamsek, G. Drazic, M. Gaberscek, N. Hodnik and P. Jovanovic, *ACS Catal.*, 2022, **12**, 15135–15145.
31 M. Bele, P. Jovanovič, Ž. Marinko, S. Drev, V. S. Šelih, J. Kovač, M. Gaberščček, G. Koderman Podboršek, G. Dražić, N. Hodnik, A. Kokalj and L. Suhadolnik, *ACS Catal.*, 2020, **10**, 13688–13700.
32 S. Zargarian, C. Roiron, G. Ferro and P. Atanassov, *ChemElectroChem*, 2025, **12**, e202400625.
33 D. Hoffmeister, S. Finger, L. Fiedler, T. C. Ma, A. Körner, M. Zlatar, B. Fritsch, K. W. Bodnar, S. Carl, A. Götz, B. A. Zubiri, J. Will, E. Spiecker, S. Cherevko, A. T. S. Freiberg, K. J. J. Mayrhofer, S. Thiele, A. Hutzler and C. van Pham, *Adv. Sci.*, 2024, **11**, 2402991.
34 C. Van Pham, M. Bühler, J. Knöppel, M. Bierling, D. Seeberger, D. Escalera-López, K. J. J. Mayrhofer, S. Cherevko and S. Thiele, *Appl. Catal., B*, 2020, **269**, 118762.
35 K. L. Ou, C. C. Weng, Y. H. Lin and M. S. Huang, *J. Alloys Compd.*, 2017, **697**, 231–238.
36 A. Kafizas, C. W. Dunnill and I. P. Parkin, *J. Mater. Chem.*, 2010, **20**, 8336–8349.
37 K. Mālnieks, S. K̦imenko, P. C. Sherrell, A. Šarakovskis, R. Eglītis, K. Šmits, A. Linarts and A. Šutka, *Adv. Mater. Interfaces*, 2025, **12**, 2400567.
38 L. R. Sheppard, T. Bak and J. Nowotny, *J. Phys. Chem. B*, 2006, **110**, 22447–22454.
39 X. Yang, Y. Min, S. Li, D. Wang, Z. Mei, J. Liang and F. Pan, *Catal. Sci. Technol.*, 2018, **8**, 1357–1365.
40 D. S. Bhachu, S. Sathasivam, G. Sankar, D. O. Scanlon, G. Cibin, C. J. Carmalt, I. P. Parkin, G. W. Watson, S. M. Bawaked, A. Y. Obaid, S. Al-Thabaiti and S. N. Basahel, *Adv. Funct. Mater.*, 2014, **24**, 5075–5085.
41 R. Badam, M. Hara, H. H. Huang and M. Yoshimura, *Int. J. Hydrogen Energy*, 2018, **43**, 18095–18104.
42 F. M. Smits, *Bell Syst. Tech. J.*, 1958, **37**, 711–718.
43 Z. Wang, X. Guo, J. Montoya and J. K. Nørskov, *npj Comput. Mater.*, 2021, 7(9), DOI: 10.1038/s41524-020-00430-3.
44 A. Kafizas, N. Noor, C. J. Carmalt and I. P. Parkin, *J. Mater. Chem. C*, 2013, **1**, 6335–6346.
45 J. Yue, C. Suchomski, P. Voepel, R. Ellinghaus, M. Rohnke, T. Leichtweiss, M. T. Elm and B. M. Smarsly, *J. Mater. Chem. A*, 2017, **5**, 1978–1988.
46 C. Kittel, *Introduction to Solid State Physics*, Wiley, 7th edn, 1965.
47 J. Murawski, S. B. Scott, R. Rao, K. Rigg, C. Zalitis, J. Stevens, J. Sharman, G. Hinds and I. E. L. Stephens, *Johnson Matthey Technol. Rev.*, 2024, **68**, 331–346.
48 J. Murawski, S. B. Scott, R. Rao, K. Rigg, C. Zalitis, J. Stevens, J. Sharman, G. Hinds and I. E. L. Stephens, *Johnson Matthey Technol. Rev.*, 2024, **68**, 31–46.
49 S. Geiger, O. Kasian, M. Ledendecker, E. Pizzutilo, A. M. Mingers, W. T. Fu, O. Diaz-Morales, Z. Li, T. Oellers, L. Fruchter, A. Ludwig, K. J. J. Mayrhofer, M. T. M. Koper and S. Cherevko, *Nat. Catal.*, 2018, **1**, 508–515.
50 J. Knöppel, M. Möckl, D. Escalera-López, K. Stojanovski, M. Bierling, T. Böhm, S. Thiele, M. Rzepka and S. Cherevko, *Nat. Commun.*, 2021, **12**, 2231.

51 D. Dorow-Gerspach, D. Mergel and M. Wuttig, *Crystals*, 2021, **11**, 301.
52 A. V. Naumkin, A. Kraut-Vass, S. W. Gaarenstroom and C. J. Powell, *NIST X-ray Photoelectron Spectroscopy Database, Version 4.1*, National Institute of Standards and Technology, Gaithersburg, MD, 2012.
53 G. Yang, Y. Zhou, M. Wang, J. Murawski, L. I. Oldham, T. Tian, I. E. L. Stephens and A. Kafizas, *ChemCatChem*, 2023, **15**, e202300687.
54 M. Abbate, J. B. Goedkoop, F. M. F. De Groot, M. Grionit, J. C. Fuggle, S. Hofmann, H. Petersen and M. Sacchi, *Surf. Interface Anal.*, 1992, **18**, 65–69.
55 L. Forro, O. Chauvet, D. Emin, L. Zuppiroli, H. Berger and F. Lévy, *J. Appl. Phys.*, 1994, **75**, 633–635.
56 C. Franchini, M. Reticcioli, M. Setvin and U. Diebold, *Nat. Rev. Mater.*, 2021, **6**, 560–586.
57 Z. Dai and F. Giustino, *Proc. Natl. Acad. Sci. U. S. A.*, 2024, **121**, e2414203121, DOI: 10.1073/pnas.2414203121.
58 G. Doo, J. Park, J. Park, J. Heo, J. Jung, D. W. Lee, H. Bae, J. Hyun, E. Oh, J. Kwen, K. M. Kim and H. T. Kim, *ACS Energy Lett.*, 2023, **8**, 2214–2220.
59 C. Liu, M. Shviro, A. S. Gago, S. F. Zaccarine, G. Bender, P. Gazdzicki, T. Morawietz, I. Biswas, M. Rasinski, A. Everwand, R. Schierholz, J. Pfeilsticker, M. Müller, P. P. Lopes, R. A. Eichel, B. Pivovar, S. Pylypenko, K. A. Friedrich, W. Lehnert and M. Carmo, *Adv. Energy Mater.*, 2021, **11**, 2002926.
60 M. F. Ernst, V. Meier, M. Kornherr and H. A. Gasteiger, *J. Electrochem. Soc.*, 2024, **171**, 074511.
61 W. Shi, T. Shen, C. Xing, K. Sun, Q. Yan, W. Niu, X. Yang, J. Li, C. Wei, R. Wang, S. Fu, Y. Yang, L. Xue, J. Chen, S. Cui, X. Hu, K. Xie, X. Xu, S. Duan, Y. Xu and B. Zhang, *Science*, **2025**, 791–796.
62 C. Daiane Ferreira Da Silva, F. Claudel, V. Martin, R. Chattot, S. Abbou, K. Kumar, I. Jiménez-Morales, S. Cavaliere, D. Jones, J. Rozière, L. Solà-Hernandez, C. Beauger, M. Faustini, J. Peron, B. Gilles, T. Encinas, L. Piccolo, F. H. Barros De Lima, L. Dubau and F. Maillard, *ACS Catal.*, 2021, **11**, 4107–4116.